Journal of *Marine Science and Engineering*

MDPI

Article

Modeling of Accidental Oil Spills at Different Phases of LNG Terminal Construction

Byoungjoon Na [1], Sangyoung Son [2,*] and Jae-Cheon Choi [3]

[1] Future and Fusion Lab of Architectural, Civil and Environmental Engineering, Korea University, Seoul 02841, Korea; bjna420@korea.ac.kr
[2] School of Civil, Environmental and Architectural Engineering, Korea University, Seoul 02841, Korea
[3] Daewoo Engineering & Construction, 170, Eulji-ro, Jung-gu, Seoul 04548, Korea; jaecheon.choi@daewooenc.com
* Correspondence: sson@korea.ac.kr; Tel.: +82-2-3290-4865

Abstract: Accidental oil spills not only deteriorate biodiversity but also cause immediate threats to coastal environments. This study quantitatively investigates the initial dispersion of spilled oil using the environmental fluid dynamics code (EFDC) model, loosely coupled with an endorsed oil spill model (MEDSLIK-II) accounting for time-dependent advection, diffusion, and physiochemical weathering of the surface oil slick. Focusing on local contributing factors (i.e., construction activities) to oil dispersion, the current model is applied to likely oil spills occurring at three different phases of the Songdo LNG terminal construction on a reclaimed site in South Korea. Applied phases pose detailed ship collision scenarios generated based on a proposed construction plan of the terminal. The effects of permeable revetments, required for reclamation, on the currents were also investigated and applied in subsequent oil spill modeling. For each scenario, the simulated results showed distinct patterns in the advection, dispersion, and transformation of the oil slick. Oil absorption into the coast, which causes immense damage to the coastal communities, is found to be highly dependent on the tidal currents, volume of oil spilled, and nearby construction activities.

Keywords: oil spill modeling; advection; dispersion; transformation; absorption; permeable revetments

Citation: Na, B.; Son, S.; Choi, J.-C. Modeling of Accidental Oil Spills at Different Phases of LNG Terminal Construction. *J. Mar. Sci. Eng.* **2021**, *9*, 392. https://doi.org/10.3390/jmse9040392

Academic Editor: Merv Fingas

Received: 27 February 2021
Accepted: 31 March 2021
Published: 7 April 2021

1. Introduction

The demand for transport facilities has dramatically increased with the rapid economic development of coastal areas, and so has the frequency of oil spill accidents [1]. Moreover, unprecedented weather conditions due to global climate change may increase the possibility of an oil spill in the ocean. These accidental oil spills often have immense impact on marine environments and coastal communities. To mitigate damage, detecting oil slick and predicting its fate (i.e., slick displacement and dispersion) often require a specific and timely intervention at sea by governmental response agencies [2]. The most renowned historical oil spills due to ship collisions include the Exxon Valdez (1989), Atlantic Empress (1979), Amoco Cadiz (1978), and Torrey Canyon (1967). The potential for maritime accidents generally increases nearshore construction sites and harbors where oil transports are frequent, and the various routes of oil tanker and barges are concurrent.

In South Korea, a peninsula where northward land transportations are limited, marine transport allows for efficient transcontinental transportation with low freight rates by enabling simultaneous transportation of large amounts of cargo. Therefore, more than 90% of the trading volume relies on marine transport, with oil traffic accounting for about 30% of all marine transportation [3]. Continuous oil-related accidents have occurred mainly due to frequent traffic and related issues. For example, an oil tanker was stranded on the reef, resulting in an oil spill of about 5000 tons near Yeosu, South Korea, in 1995. In 2007, the Hebei Spirit oil spill accident was occurred near Manripo beach, Taean, in the

Yellow Sea, with a leakage of about 10,900 tons of cargo oil, which was recorded as the largest marine oil spill in South Korea [3]. This incident was triggered by a crane barge, "Samsung 1", losing moored connections with a tugboat and subsequently crashing onto the oil tanker, "Hebei Spirit". The spilled oil spread rapidly, mainly due to the strong northwestern winds and currents, making initial recovery almost impossible and thereby contaminating more than 375 km of coastlines on the west coast of South Korea. The Ministry of Oceans and Fisheries of South Korea initially reported that the spilled oil would reach the coast within 24 h. However, it was later found that the spilled oil reached the coast within 13 h because of harsh weather and associated strong winds and currents. Such unprecedented oil absorption into the coast caused destruction of marine ecosystems and further increased the cost of damage compensation and cleaning up the spilled oil. Therefore, numerous studies have been conducted to refine and enhance oil spill models to reduce this discrepancy between the predicted and the actual trajectories of spilled oil.

To predict the drift and dispersion of the oil spills, various numerical models have been developed. BLOSOM (Blowout and Spill Occurrence Model) was developed by the US Department of Energy to model the fate and transport of both subsurface oil blowouts and surface spills. GNOME (General NOAA Operational Modeling Environment) was built by the US National Oceanic and Atmospheric Administration to predict the potential trajectory of offshore pollutants on the sea surface [4]. Duran et al. [5] showed that BLOSOM provided a closer match with the observation compared with GNOME, mainly due to the inclusion of an internally computed deflection angle for wind-driven advection. More oil spill prediction models, including the TESEO-PICHI [6], COZOIL [7], SINTEF OSCAR 2000 [8], OILMAP [9], GULFSPILL [10], ADIOS [11], MOTHY [12], MOHID [13], the POSEIDON OSM [14], and OD3D [15], span a range of well-developed systems, both from the industry and academia [16]. In all these models, equations and approximations are seldom given, and the results are given as the position of the oil slick particles and time evolution of the total oil volume [17].

MEDSLIK-II, a Lagrangian marine surface oil spill model for short-term forecasting, adopted by the Regional Marine Pollution Emergency Response Center for Mediterranean, simulates the fate of oil in the environment based on Lagrangian transport of the spilled oil slick coupled with weathering factors [17,18]. Unlike the aforementioned oil spill models, MEDSLIK-II reconstructs an oil concentration field from the oil particles' advection-diffusion and transformation (i.e., weathering) processes. Moreover, De Dominicis et al. [17] provided a comprehensive explanation of all the possible corrections to be applied to the ocean current fields, and thus a coupling process with operational hydrodynamics models is relatively simple. For this reason, MEDSLIK-II has been used operationally for daily forecasts of the oil spilled during the Lebanon oil pollution incident in 2006, which is considered as the biggest oil pollution in the Eastern Mediterranean [19,20].

This paper presents simulated results of transport, diffusion, and transformation of surface oil using MEDSLIK-II. Tidal and wind drift currents were computed using the environmental fluid dynamics code (EFDC) model. The simulation was conducted under three scenarios determined based on a proposed construction plan of the Songdo LNG terminal, which was built on reclaimed land near the west coast of Incheon, South Korea [21]. For the case study, the three most likely scenarios have been chosen considering distinguished construction stages with corresponding terminal architectures, vessel numbers, locations, types, sizes, and navigation routes to closely reflect the three progressing construction stages from phase 1 to phase 3. Section 2 describes the adopted scenarios and numerical approaches employed. In Section 3, the simulation results are first verified by the observed data and then presented and discussed, focusing on variations in the current fields and oil concentrations depending on detailed construction stages.

2. Numerical Models

The current oil spill model was constructed by loosely (one-way) coupling EFDC [22] for computing tidal elevation and current fields to MEDSLIK-II [17] to predict oil slick

advection-diffusion and transformation processes [21]. Wind velocity fields, computed based on extreme value analysis utilizing the probability density function of a 5-year easterly wind, were also fed into MEDSLIK-II, accounting for atmospheric conditions (Figure 1). To investigate initial dispersion, 12-h current velocity fields computed from EFDC during maximum phases of ebb to flood at spring tide were inputted to MEDSLIK-II. For efficient data transfer, a spatial grid resolution of 10 m and a time step of 6 min were set for both EFDC and the MEDSLIK-II. Since the computations in EFDC are based on the Eulerian coordinate system, compared with the Eulerian/Lagrangian coordinate system used in MEDSLIK-II, a coordinate conversion was required and applied in the current study to collocate the nodes. Specifically, MEDSLIK-II firstly computes transport, diffusion, and transformation of surface oil in the Eulerian coordinate system based on the Eulerian-based current fields from EFDC, which are then utilized to compute oil spill model state variables [17], including oil concentration and oil slick state variables. As a result, forecasts of oil spill transport and transformation are enabled through the Lagrangian representation of advection-diffusion processes and oil slick variables for weathering processes.

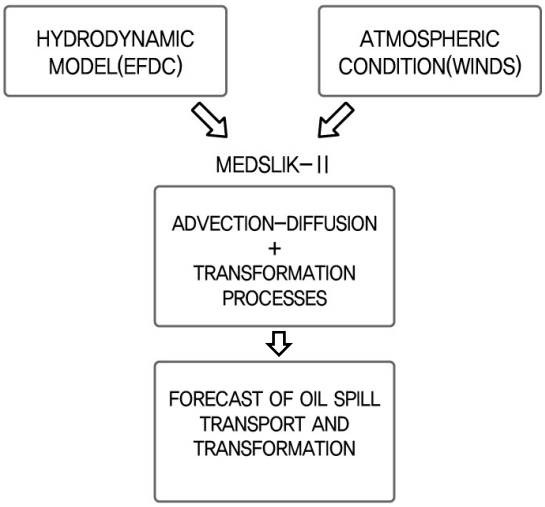

Figure 1. Schematic of the oil spill model (MEDSLIK-II) applied in the current study.

2.1. Numerical Domain and Selected Scenarios

To provide hydrodynamic conditions, EFDC calculated the tidal and wind-induced currents at each construction stage (Daewoo E&C, 2019). Figure 2a,b shows the bathymetry and corresponding orthogonal curvilinear grid system in an expanded domain encompassing approximately 130 km in the east-west and 200 km the south-north directions applied in the current study. The grid size varies from 10 ~ 500 m with finer resolutions set close to the LNG terminal construction site (Figure 2c,d). The total number of valid computational grids is 34,408. Five vertical layers (1: surface; 2~4: middle; and 5: bottom) were constructed through the model. The current EFDC model was run for 30 days with a temporal resolution of 3 s. The modeled tide was decomposed to four major tidal constituents including M_2, S_2, K_1, and O_1.

Three ship collision scenarios were generated based on a proposed construction plan of the Songdo LNG terminal that is expected to be built on reclaimed land, as depicted in Figure 3. The three scenarios are essentially representative of the three distinguished construction phases (phase 1, 2, and 3) depending on the time frames of construction. Thus, configurations of the construction vessels and probable hazards were reconstructed accordingly. Similar to the Hebei Spirit oil spill accident, an oil spillage was assumed to have originated from a fuel tanker for each scenario (Figure 3). In phase 1, an oil spill of 29,400 L was initiated near the western revetment due to the collision of the fuel tanker. In phase 2 and phase 3, 23,100 and 10,500 L of oil were spilled, both near the eastern revetment, due to the collision of the fuel tanker. A list of the selected properties of the

fuel tanker for each scenario is provided in Table 1. A gradual spill of Low-Sulfur Fuel Oil (LSFO) with a prescribed constant spill rate for a 1-h time span was set, derived from the total volume of the spilled oil being 70% of the tanker capacity for all scenarios. Sample properties of LSFO applied in the current model are a density of 0.91 tonne/m^3, a viscosity of 95.50 mm^2/s at 15 °C, and a vapor pressure of 0.184 bar. Note that this gradual spill condition improves the relatively unrealistic oil spill scenarios with an instantaneous total spill condition applied in Lee et al. [3]. To evaluate the model predictability, the predicted tidal elevation and current speeds were compared to the observed data by the Korea Hydrographic and Oceanographic Agency. The validation was executed in the vicinity of the construction site at two points (T1 and T2) for the tidal elevation and three points (PC1, PC2, and PC3) for the current speed, as shown in Figure 2e.

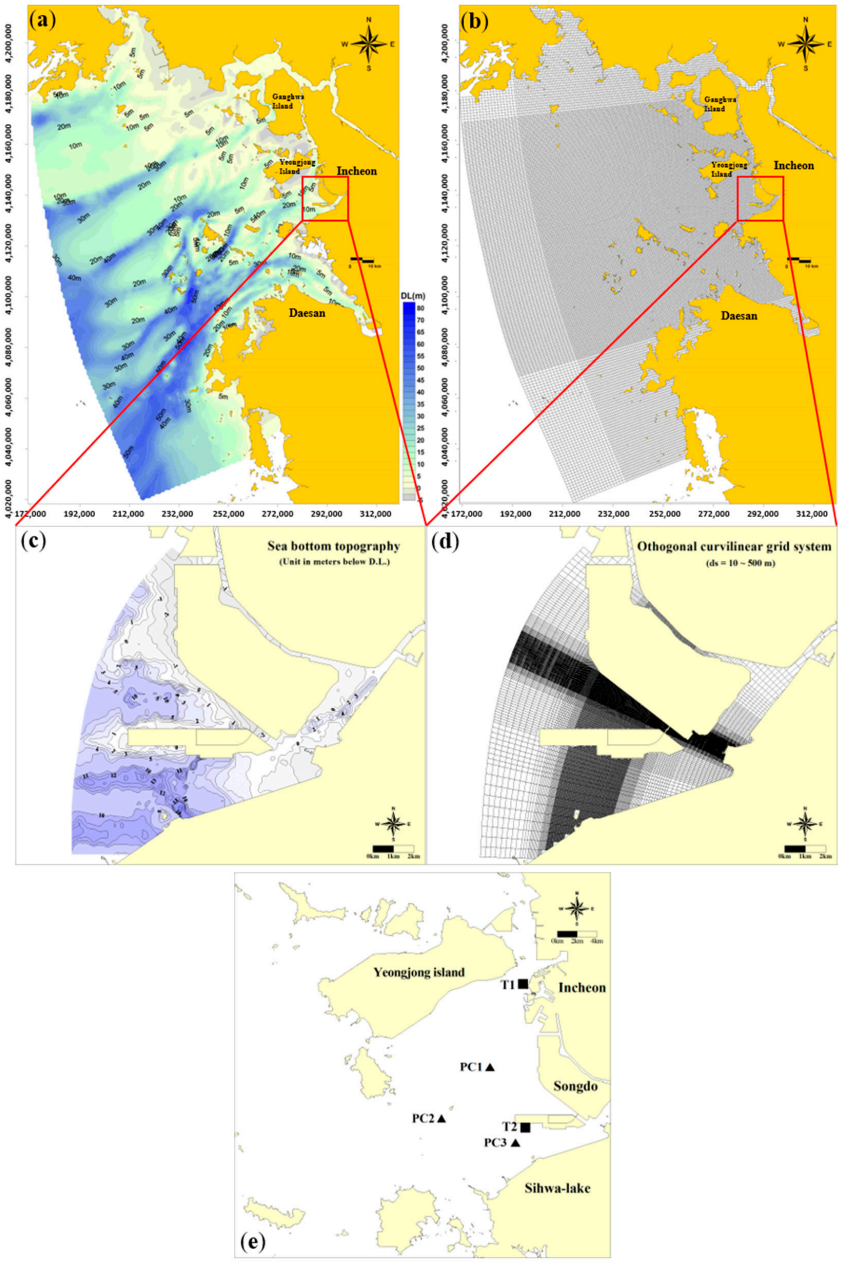

Figure 2. Bathymetry contours in meters in the (**a**) expanded and (**c**) detailed domain. The extent of a multilayered orthogonal curvilinear grid system in the (**b**) expanded and (**d**) detailed domain. (**e**) Enlarged view of target area. T1-T2 indicate the locations of the tidal elevation stations, and PC1-PC3 indicate the locations of the tidal current stations.

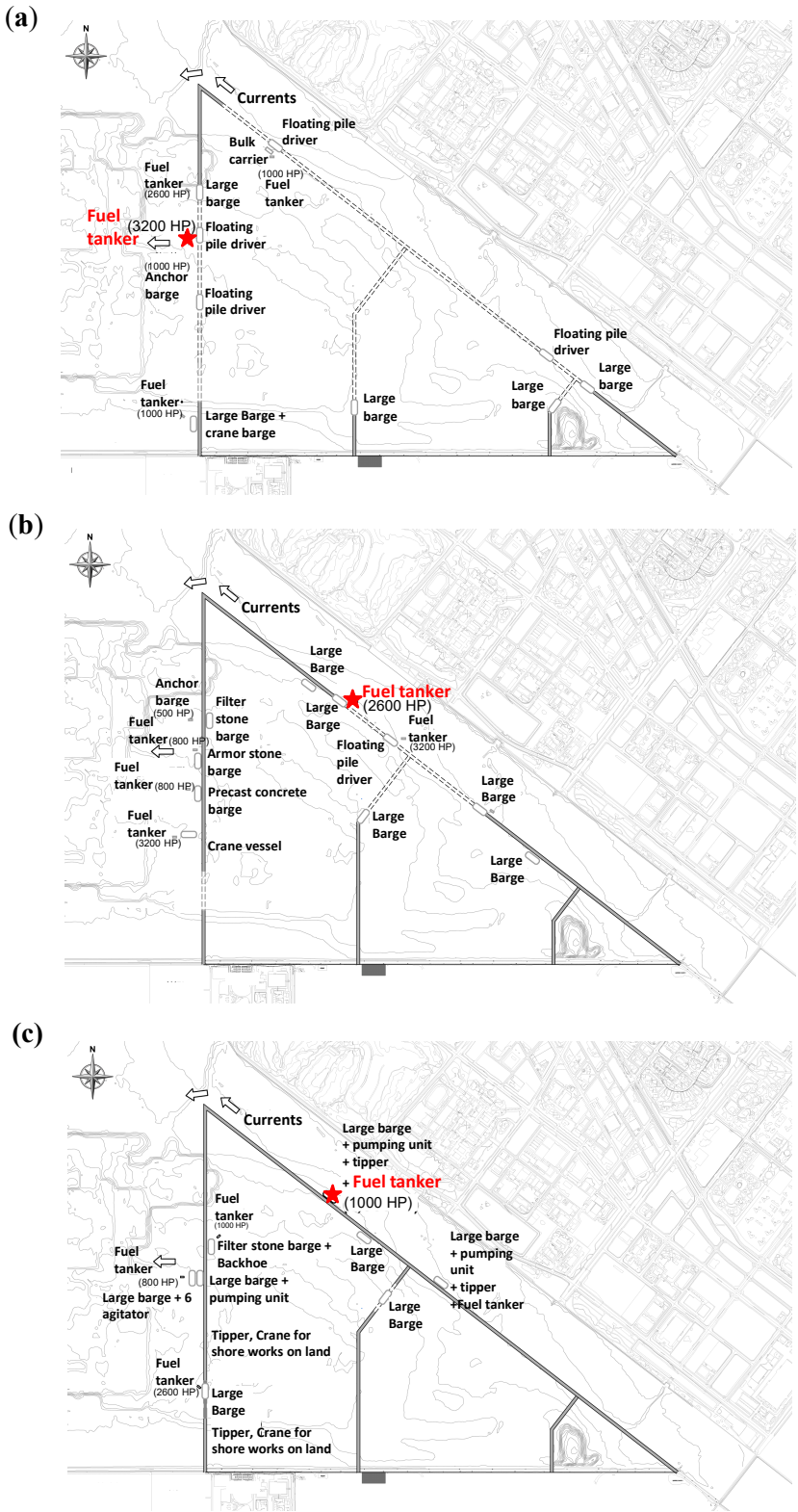

Figure 3. Ship collision scenarios based on a proposed construction plan of the Songdo LNG terminal in (**a**) phase 1, (**b**) phase 2, and (**c**) phase 3. The three most likely scenarios have been chosen by considering distinguished construction stages with corresponding terminal architectures, vessel numbers, locations, types, sizes, and navigation routes. For each scenario, a collision symbol (a star in red) is included to highlight the location at which the oil spill is initiated.

Table 1. Selected volumes of the fuel tanker for each scenario used in the current study. The spilled oil volume is assumed to be approximately 70% of the tanker capacity in the fuel tanker.

Scenario	Vessel Horsepower (HP)	Tanker Capacity (L)	Oil Spillage Volume (L)	Initial Spill Location
1	3200	42,000	29,400	Western revetment
2	2600	33,000	23,100	Eastern revetment
3	1000	15,000	10,500	Eastern revetment

2.2. Hydrodynamic Model

The EFDC model solves the three-dimensional primitive equations of motion for turbulent flow in a horizontal curvilinear-orthogonal and vertical σ-stretched coordinate system [23]. Transforming the vertically hydrostatic boundary layer form of the turbulent equations of motion and utilizing the Boussinesq approximation for variable density provides the following forms of continuity equation and momentum equations [22]. The continuity equation is

$$\partial_t(m_x m_y H) + \partial_x(m_y HU) + \partial_y(m_x HV) + \partial_z(m_x m_y W) = 0, \quad (1)$$

where m_x and m_y are the horizontal scale factors; H is the sum of the mean water depth (h) and free surface elevation (ζ) $H = h + \zeta$; U and V are the horizontal velocity components in the curvilinear, orthogonal coordinates x and y, respectively; and W is the vertical velocity in the σ-stretched dimensionless vertical coordinate z [22].

The momentum equations are

$$\begin{aligned}\partial_t(m_x m_y HU) + \partial_x(m_y HUU) + \partial_y(m_x HVU) + \partial_z(m_x m_y WU) - f_e m_x m_y HV \\ = -m_y H\partial_x(g\zeta + P) + m_y(\partial_x z + z\partial_x H)\partial_z P + \partial_x\left(m_x m_y \tfrac{A_v}{H}\partial_z U\right) + Q_u,\end{aligned} \quad (2)$$

$$\begin{aligned}\partial_t(m_x m_y HV) + \partial_x(m_y HUV) + \partial_y(m_x HVV) + \partial_z(m_x m_y WV) + f_e m_x m_y HU \\ = -m_x H\partial_y(g\zeta + P) + m_x(\partial_y z + z\partial_y H)\partial_z P + \partial_x\left(m_x m_y \tfrac{A_v}{H}\partial_z V\right) + Q_v,\end{aligned} \quad (3)$$

where f_e is the Coriolis parameter; g is the gravitational acceleration; P is the pressure; A_v is the vertical eddy viscosity, determined based on the second moment turbulence closure model [24,25]; Q_u and Q_v are the source and sink terms, respectively. Further details of the above formulations and numerical techniques employed in the EFDC model are provided in Hamrick [22].

2.3. Oil Spill Model

In the current study, MEDSLIK-II [17] is employed to simulate the processes of transportation, diffusion, and transformation of surface oil in seawater. In MEDSLIK-II, a tracer concentration, with units of mass over volume, mixed in the marine environment is formulated as

$$\frac{\partial C}{\partial t} + \boldsymbol{U}\cdot\nabla C = \nabla\cdot(\boldsymbol{K}\nabla C) + \sum_{j=1}^{M} r_j(x, C(x,t), t), \quad (4)$$

where $\partial/\partial t$ is the local time-rate-of-change operator, $\boldsymbol{U}$ is the sea current mean field with components (U, V, W), $\boldsymbol{K}$ is the diffusivity tensor which parameterizes the turbulent effects, and $r_j(C)$ are the M transformation rates that modify the tracer concentration by means of physical and chemical transformation processes.

$$\frac{\partial C_1}{\partial t} = \sum_{j=1}^{M} r_j(x, C(x,t), t), \quad (5)$$

$$\frac{\partial C}{\partial t} = U\cdot\nabla C_1 + \nabla\cdot(\boldsymbol{K}\nabla C_1), \quad (6)$$

where C_1 is the oil concentration solution solely due to the weathering process, while the final time rate of change of C is given by the advection-diffusion acting on C_1. Considering the oil volume, density ρ, and unit area A, the surface oil concentration (C_S) and the dispersed oil concentration (C_D), with units of kg m^{-2}, can be defined as

$$\begin{array}{l} C_S(x,y,t) = \frac{\rho}{A} V_S \\ C_D(x,y,t) = \frac{\rho}{A} V_D, \end{array} \quad (7)$$

$$\begin{array}{l} \frac{dC_S}{dt} = \frac{\rho}{A} \frac{dV_S}{dt} \\ \frac{dC_D}{dt} = \frac{\rho}{A} \frac{dV_D}{dt}, \end{array} \quad (8)$$

where vs. and V_D are the surface and dispersed oil volumes. When the surface oil arrives close to the coasts, defined by a reference segment L_C, the oil can be absorbed and the concentration of oil at the coasts, C_C, is defined as

$$C_C(x,y,t) = \frac{\rho}{L_C} V_C, \quad (9)$$

where V_C is the absorbed oil volume. In order to use the [26] transformation algorithms, the surface volume, V_S, is subdivided into a thin part, V^{TN}, and a thick part, V^{TK}, as

$$V_S = V^{\mathrm{TN}} + V^{\mathrm{TK}}, \quad (10)$$

where

$$\begin{array}{l} V^{\mathrm{TN}}(x,y,t) = A^{\mathrm{TN}}(t) T^{\mathrm{TN}}(x,y,t) \\ V^{\mathrm{TK}}(x,y,t) = A^{\mathrm{TK}}(t) T^{\mathrm{TK}}(x,y,t). \end{array} \quad (11)$$

Here, A^{TN} and A^{TK} are the areas occupied by the thick and thin surface slick volume, and T^{TN} and T^{TK} are the thicknesses of the thick and thin surface slicks.

To solve the advection-diffusion process (Equation (6)) and compute C_{S} (Equation (7)), C_{D} (Equation (7)), and C_C (Equation (9)), the surface volume is broken into N constituent particles that are characterized by a particle volume index, $v(n_{\mathrm{k}},t)$, particle status index, $\sigma(n_{\mathrm{k}},t)$, and particle position vector $\boldsymbol{x}_k(n_{\mathrm{k}},t)$ defined as

$$\boldsymbol{x}_k(n_k,t) = (x_k(n_k,t) + y_k(n_k,t) + z_k(n_k,t)), \quad k = 1,N, \quad (12)$$

where n_k is the particle identification number. Following uncoupled Langevin equations, the time evolution of the particle position vector $\boldsymbol{x}_k(n_{\mathrm{k}},t)$ is given as

$$\frac{dx_k(t)}{dt} = \boldsymbol{A}(x_k,t) + \boldsymbol{B}(x_k,t)\xi(t) \frac{dx_k(t)}{dt} = \boldsymbol{A}(x_k,t) + \boldsymbol{B}(x_k,t)\xi(t), \quad (13)$$

where the tensor $\boldsymbol{A}(\boldsymbol{x}_k,t)$ represents the deterministic part (i.e., $\boldsymbol{U}$ in Equation (4)), while the tensor $\boldsymbol{B}(\boldsymbol{x}_k,t)$ and $\boldsymbol{\xi}$(t) characterizing random motion and a random motion factor represent the stochastic part of the flow field. Furthermore, the particle volume index, $v(n_{\mathrm{k}},t)$, is subdivided into evaporative, $v_E(n_{\mathrm{k}},t)$, and non-evaporative, $v_{NE}(n_{\mathrm{k}},t)$, particle volume attributes as follows:

$$v(n_k,t) = v_E(n_k,t) + v_{NE}(n_k,t). \quad (14)$$

The particle volume index, $v(n_{\mathrm{k}},t)$, is updated using empirical formulas that relate to the time rate of change of oil slick volume state variables. The particle status index, $\sigma(n_{\mathrm{k}},t)$, identifies the four particle classes (i.e., particles on the surface, subsurface or dispersed particles, sedimented particles, particles on the coasts). Further details of the expansion of Equation (10) and the description of the time rate of oil slick volume state variables are explained in De Dominicis et al. [17]. The above processes are summarized in a flowchart as shown in Figure 4.

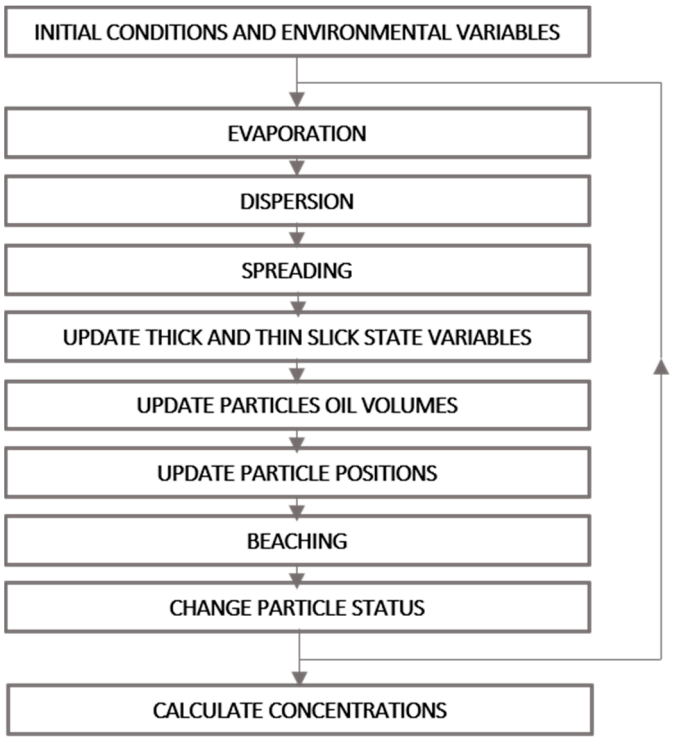

Figure 4. Computation flowchart in MEDSLIK-II.

3. Results and Discussion

3.1. Model Verification

3.1.1. Tidal Elevation and Current

To validate the model in the target area (Figure 2e) prior to the construction of the LNG terminal, Table 2 lists the comparisons of the amplitudes and the phases of the tidal constituents between the computed and observed data [21]. Overall, the comparisons are in close accordance with absolute relative errors of 2.0% and 2.5% at T1 and T2, respectively. In Table 2, noticeable discrepancies of tidal amplitudes at T2, near the bottom of the reclaimed land (Figure 2e), may be due to the effects of surf-zone waves and associated intermittent breaking, which is not considered in the model. Breaking-induced splash-ups and droplets often cause spikes in the output signals, for example [27]. Nevertheless, Figure 5 shows that tidal elevations are generally in close match, even at T2, implying that the model is capable of predicting the total tidal elevation, its peaks and its temporal variations fairly accurately.

Table 2. Computed tidal elevations using the environmental fluid dynamics code (EFDC) model compared with the corresponding observed data at (a) T1 and (b) T2.

Tidal Elevation		Amplitude (cm)		Phase (°)		Approximation Relative Error (%)
Gauge Station	Constituents	Observed	Computed	Observed	Computed	
T1	M_2	286.2	279.3	141.4	138.5	2.0
	S_2	112.7	110.6	201.6	197.7	
	K_1	39.4	39.1	306.8	305.8	
	O_1	25.2	25.4	265.7	266.6	
T2	M_2	278.5	127.5	274.0	134.0	2.5
	S_2	112.6	184.3	108.6	192.0	
	K_1	38.8	301.7	39.2	302.8	
	O_1	28.5	262.1	25.2	263.5	

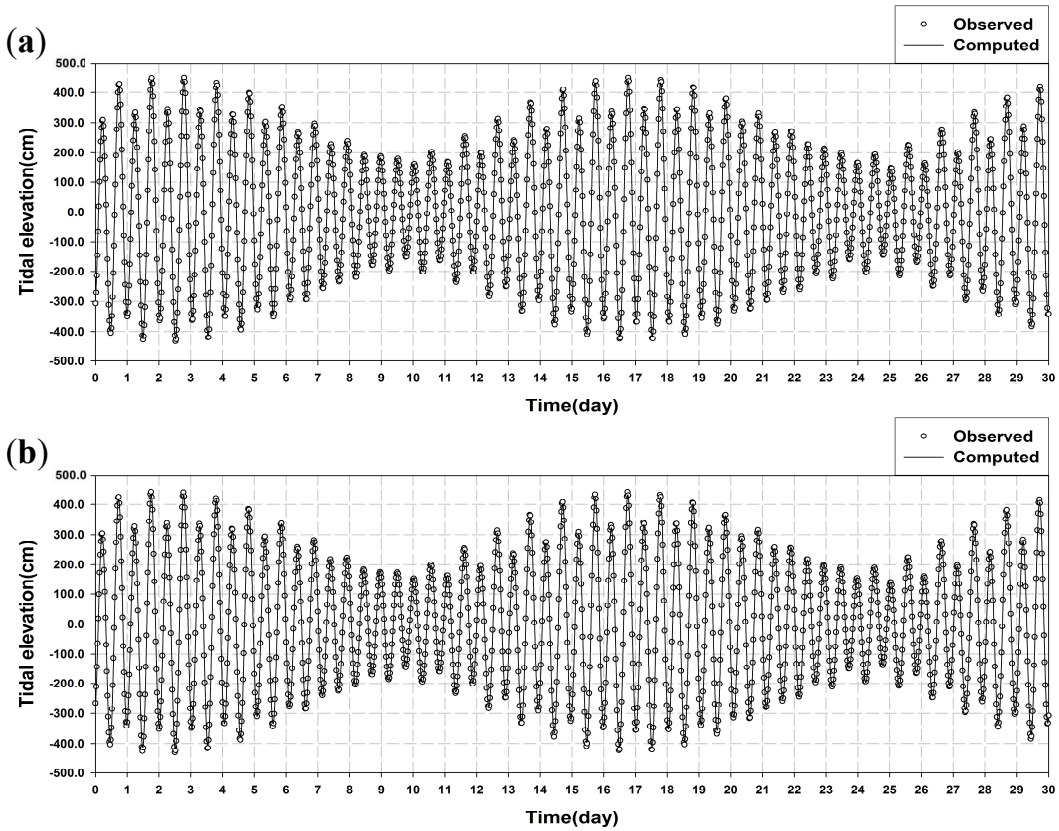

Figure 5. Computed tidal elevations using the EFDC model compared with the corresponding observed data at (**a**) T1 and (**b**) T2.

Tables 3 and 4 and Figure 6 show the comparisons of the computed and observed eastward (U) and northward (V) current velocity components for the major tidal constituents M_2, S_2, K_1, and O_1. For all the gauge stations, the amplitude approximation error, E_{app}, i.e., $\left(A_{obs} - A_{comp}\right)/A_{comp} \times 100$, where A_{obs} and A_{comp} are the observed and computed amplitudes, averaged over the four tidal constituents, was below 10%, which indicates that, in general, the computed amplitudes and phases of the tidal currents did not deviate intensely from the observed data except for PC2.

Table 3. Computed eastward tidal velocity components using the EFDC model compared with the corresponding observed data at PC1, PC2, and PC3.

Horizontal Velocity (U)		Amplitude, A (cm/s)		Phase, θ (°)		Approximation Relative Error, E_{app} (%)
Gauge Station	Constituents	Observed	Computed	Observed	Computed	
PC1	M_2	59.2	57.9	45.8	46.6	−0.3
	S_2	20.3	23.5	105.7	106.2	
	K_1	6.6	5.0	238.1	217.1	
	O_1	3.1	3.1	188.5	183.9	
PC2	M_2	34.1	33.6	38.9	50.0	−8.3
	S_2	9.9	17.5	281.4	307.7	
	K_1	4.1	3.2	217.8	217.8	
	O_1	3.8	1.9	232.6	182.0	
PC3	M_2	28.8	29.8	95.2	94.5	−6.3
	S_2	12.9	16.8	172.3	180.1	
	K_1	4.2	3.8	296.0	300.9	
	O_1	3.5	2.1	274.2	274.9	

Table 4. Computed northward tidal velocity components using the EFDC model compared with the corresponding observed data at PC1, PC2, and PC3.

Vertical Velocity (V)		Amplitude, A (cm/s)		Phase, θ (°)		Approximation Relative Error, E_{app} (%)
Gauge Station	Constituents	Observed	Computed	Observed	Computed	
PC1	M_2	26.3	24.5	57.8	42.8	3.1
	S_2	8.3	9.7	110.1	103.3	
	K_1	2.9	2.2	251.2	217.1	
	O_1	1.7	1.6	204.0	170.7	
PC2	M_2	34.3	33.2	45.5	50.2	9.7
	S_2	15.7	13.1	30.9	39.5	
	K_1	4.5	2.4	219.7	217.8	
	O_1	1.0	1.4	15.8	15.0	
PC3	M_2	7.3	7.0	111.6	121.4	3.6
	S_2	3.5	4.0	193.1	188.7	
	K_1	1.7	1.5	296.0	300.0	
	O_1	1.3	0.8	30.9	33.2	

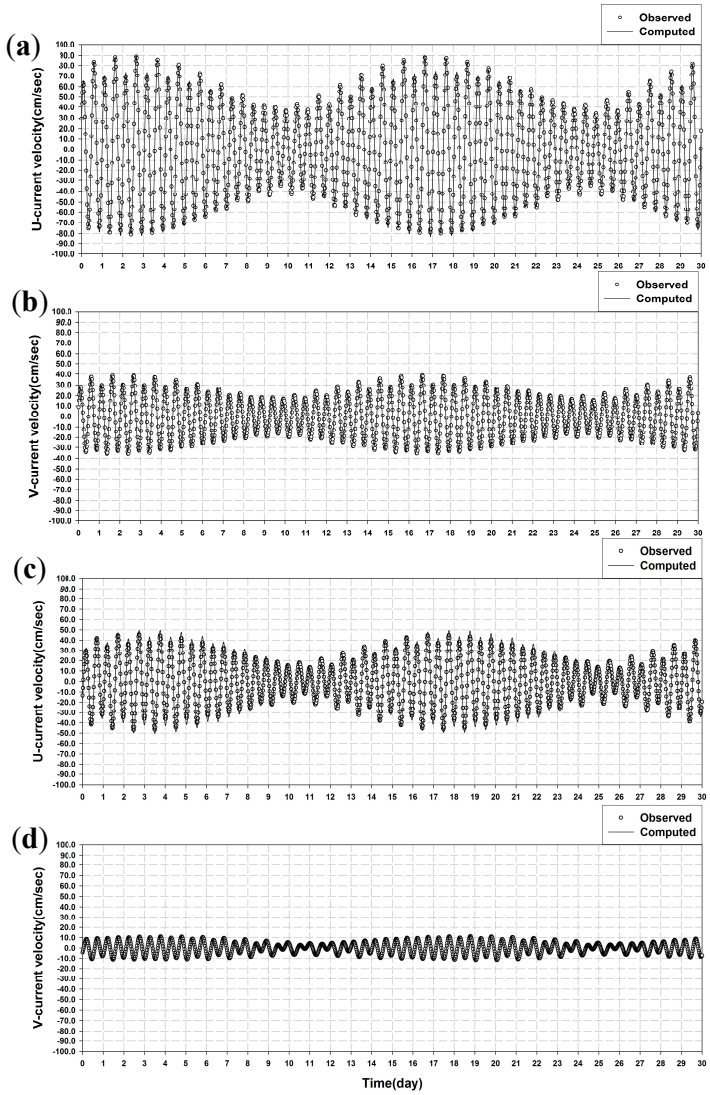

Figure 6. Comparison of the temporal variations of the observed horizontal (U) and vertical (V) current velocity components at (**a**,**b**) PC2 and (**c**,**d**) PC3.

3.1.2. Residual Current

To better investigate the hydrodynamic model's predictability of time-invariant tidal characteristics, the trajectories of the residual currents and the resultant average velocity magnitudes and directions were compared at the surface, middle and bottom layers (1, 3, 5) between the compared and observed data [21]. Residual currents are basically defined as the currents averaged over corresponding tidal periods [28]. Figures 7 and 8 depict the comparison of the trajectories and the resultant magnitudes and directions of the average velocities of the residual currents between the computed and observed data at PC2 and PC3, respectively. The comparison clearly shows that the EFDC model employed in the current study is successfully applicable in predicting residual currents not only on the surface but also at subsurface layers.

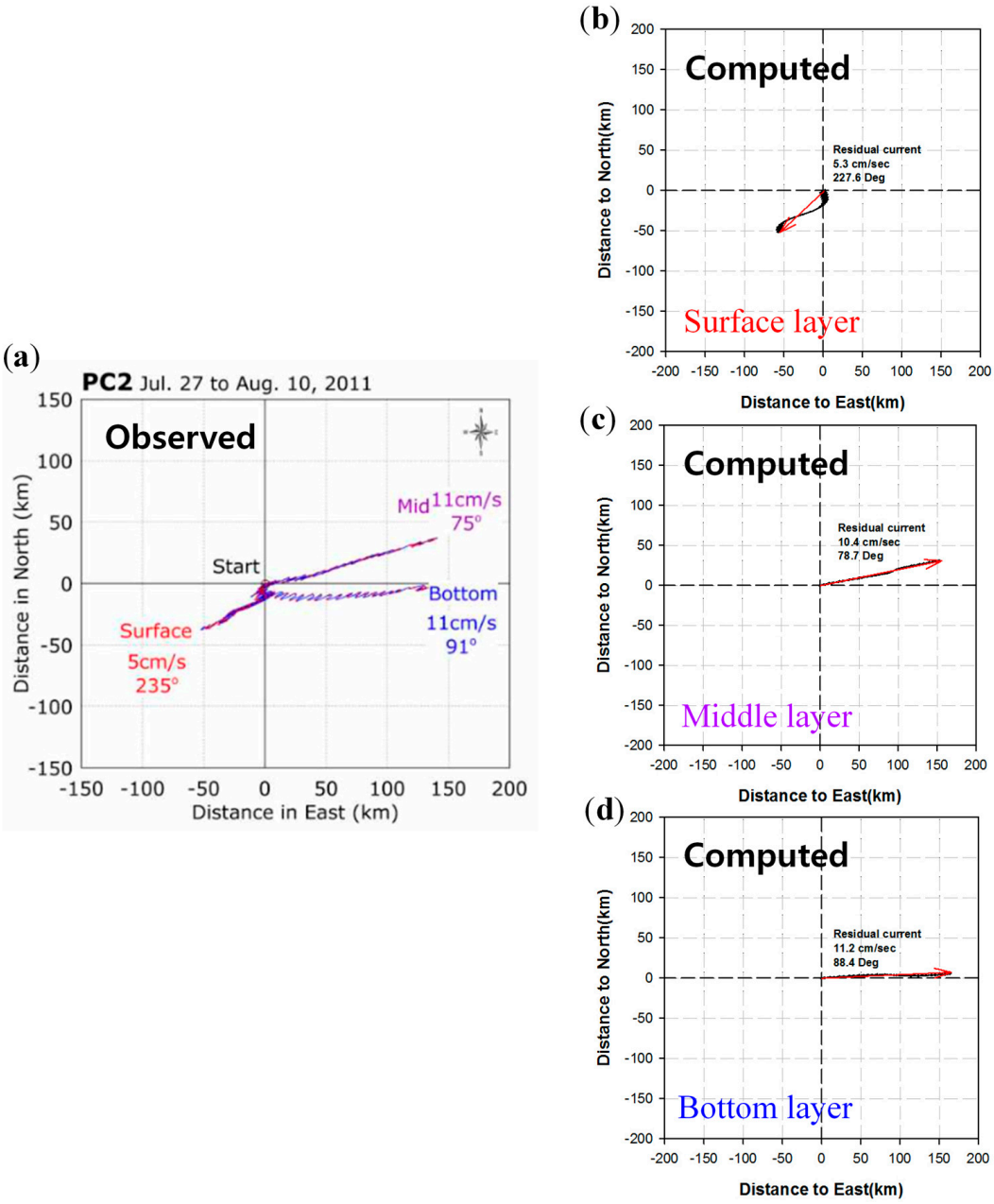

Figure 7. Comparison of the trajectories and the resultant magnitudes and directions of the average velocities of the residual currents between the (**a**) observed and the (**b**–**d**) computed data at PC2.

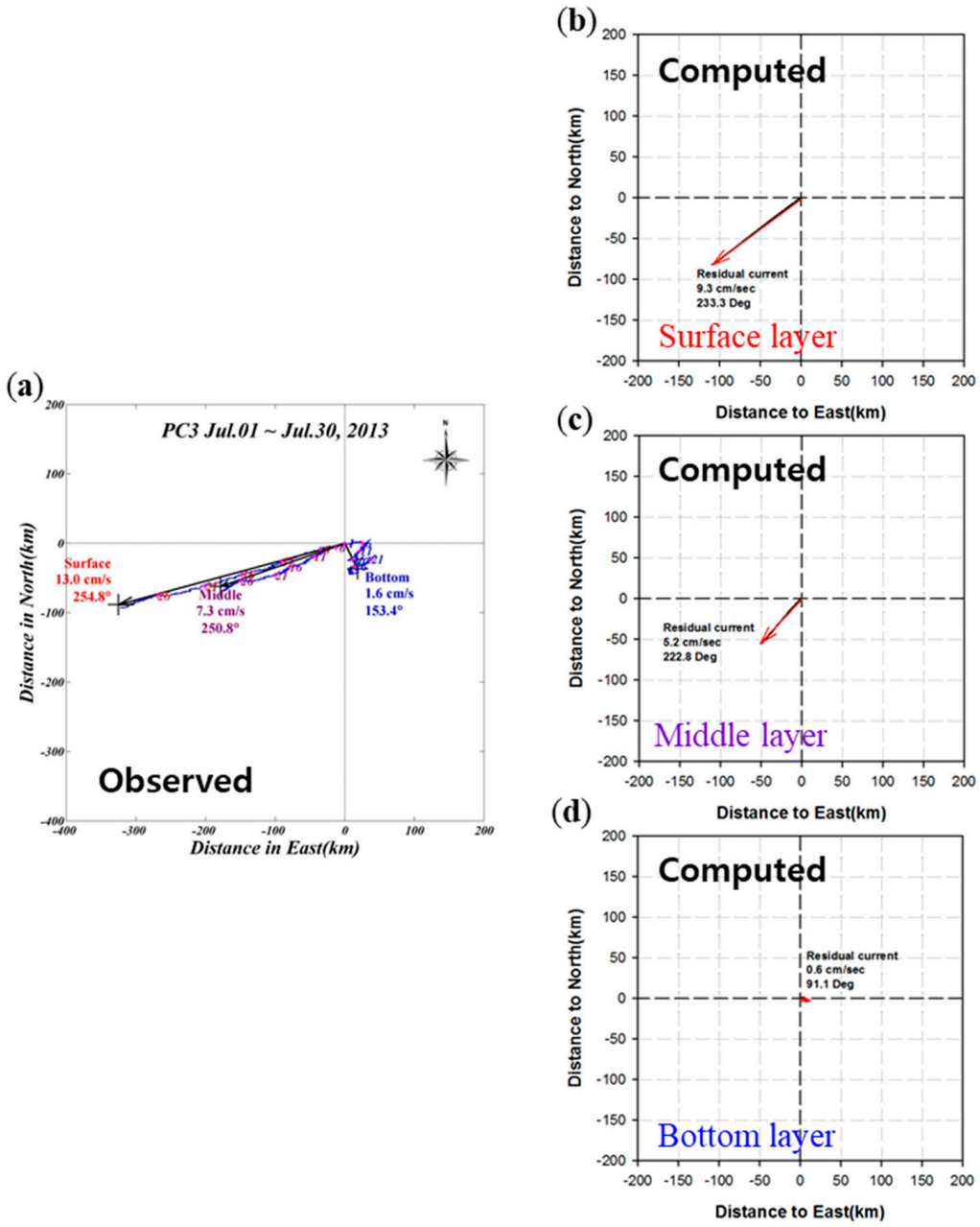

Figure 8. Comparison of the trajectories and the resultant magnitudes and directions of the average velocities of the residual currents between the (**a**) observed and the (**b**–**d**) computed data at PC3.

3.2. Tidal Currents Variation Considering Permeable Revetments

3.2.1. Water Circulation through Permeable Revetments

Port developments and reclamations are prevalent in South Korea due to the high population density. Therefore, revetment constructions are also in high demand around coastal regions, including the current Songdo LNG terminal area. Since the oil dispersion modeling in the current study needs accurate current prediction as an input in the presence of revetments, as depicted in the three scenarios (Figure 3), variation in the current fields in conjunction with revetment construction stages needs to be investigated. Since most of these revetments are permeable, even if the revetments are completely closed, the sea water circulates in and out of the embankments. Therefore, tidal elevation in areas surrounded

by revetments also varies depending on tidal cycles and should be considered. To account for this permeability of the sea dike, Dupuit parabola [29] is employed as follows

$$A_C \frac{\Delta h_0}{\Delta t} = QL, \tag{15}$$

where A_C denotes a closed area surrounded by sea dikes, h_0 is the tidal elevation outside A, Q is the circulation flow rate per unit length of dike, and L is the total length of dike (Figure 9). In LHS of Equation (15, the time rate of change in h_0 is used because the permeability coefficient varies depending on the elevations both inside and outside of the revetments. Data for the time rate of change in h_0 were provided by Korean Ministry of Oceans and Fisheries.

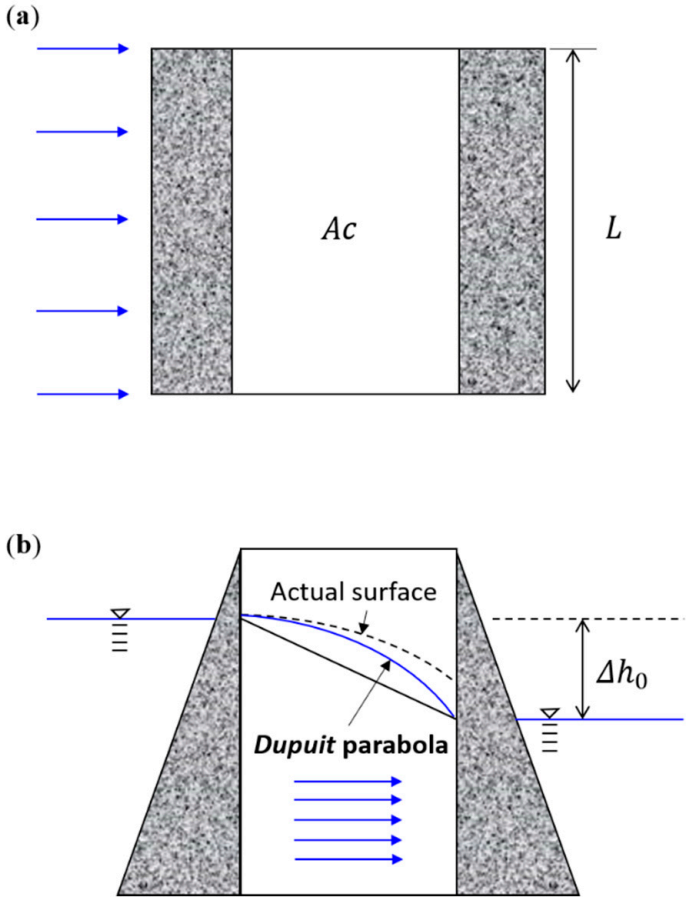

Figure 9. Schematic of the groundwater flow through permeable sea-dyke in (**a**) plan view and (**b**) side view.

Figure 10 shows the selected locations of the inside and outside of the western revetment used for comparison. Three passages for an additional seawater exchange were considered, as depicted in Figure 10, to reduce the possible instability of the revetment caused by uneven hydrostatic pressure on each side, especially under harsh weather conditions. Table 5 shows the modeling results with and without the installation of the three passages. When the additional passages were installed, the difference in the predicted tidal elevations at T3 and T4 are decreased approximately to half, indicating that the passage installation is effective in enhancing revetment stabilities.

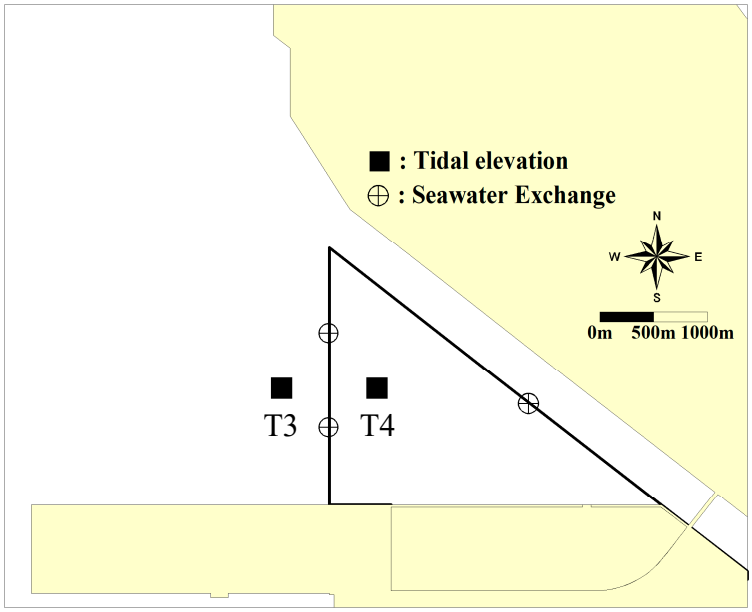

Figure 10. Locations of the station inside and outside the revetment for comparison of the modeled results. Circles indicate the locations of the passage deployments for an additional seawater exchange consideration.

Table 5. Comparison of the computed tidal elevation at high tide with and without the installation of the three passages at T3 and T4.

Condition	Tidal Elevation at High Tide (m)		Δh_0 (m)
	T3	T4	
Without passage	9.19	7.73	1.46
With passage	9.19	8.37	0.82

3.2.2. Tidal Current Velocity Fields

Considering the permeability of the sea dike, the current velocity fields were predicted through the EFDC model. The three initial conditions (i.e., case 1: without dike; case 2: with dike only; and case 3: with both dike and passage) were applied in the model. Figure 11a,b shows the current velocity fields in the enlarged view, as in Figure 2e, at the pre-construction stage before the sea dikes are built. The flood current fields are dominantly directed northeast, while the ebb current is generally directed in the opposite direction to southwest. Due to the combined effects of geometry and bathymetry, the primary current direction near the construction site is east-west in direction (Figure 11c,d). The maximum velocities in the detailed domain near construction site during the initial dispersion phase of the 12-h time frame were 0.12–0.59 m/s on the surface (layer 1). At layers 3 and 5, the maximum velocities decreased to 0.11–0.56 m/s and 0.09–0.49 m/s, respectively (current fields not shown for brevity in Figure 11).

Figure 12 shows the current fields assuming that only the revetments were constructed completely without allowing passages for additional direct seawater exchanges (case 2). The dominant directions of the tidal currents were more or less similar in direction, indicating that the effects of revetments on the major current direction are not crucial in the study area (Figures 11b and 12a). On the other hand, the maximum velocities near the construction site were significantly reduced to 0.04–0.27 m/s on the surface, as depicted by Figure 12c,d. Note that variations in the maximum values of tidal currents considering the permeable sea dikes are significant, especially at the northern end of the waterway, with and without considering the revetments.

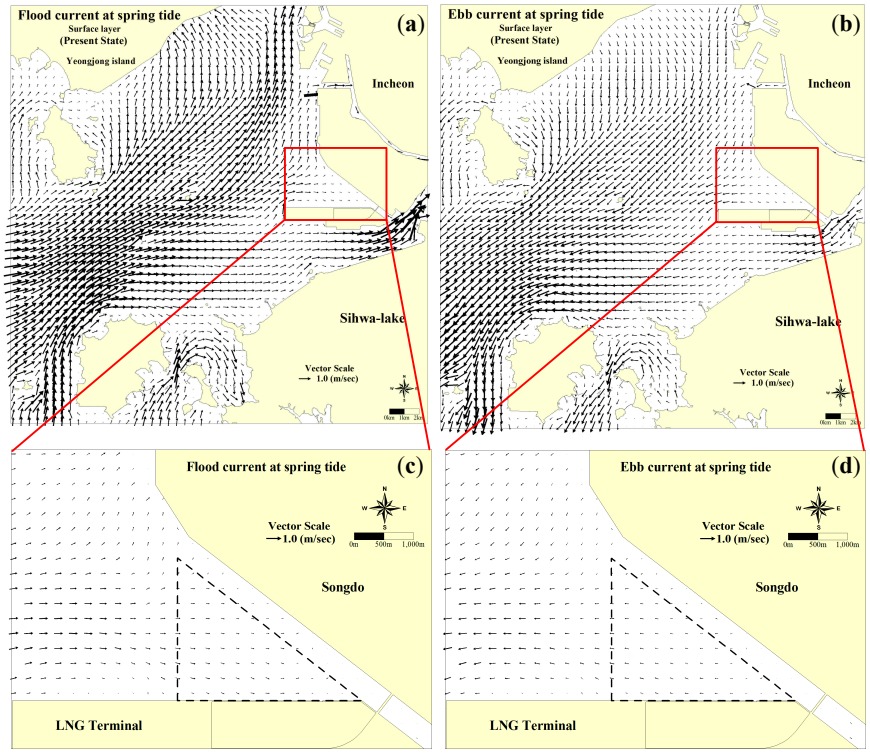

Figure 11. Current velocity fields in case 1 during the pre-construction phase without revetments installed. Current fields are shown in the enlarged views during (**a**) flood and (**b**) ebb and in the detailed domain near the LNG terminal construction site during (**c**) flood and (**d**) ebb.

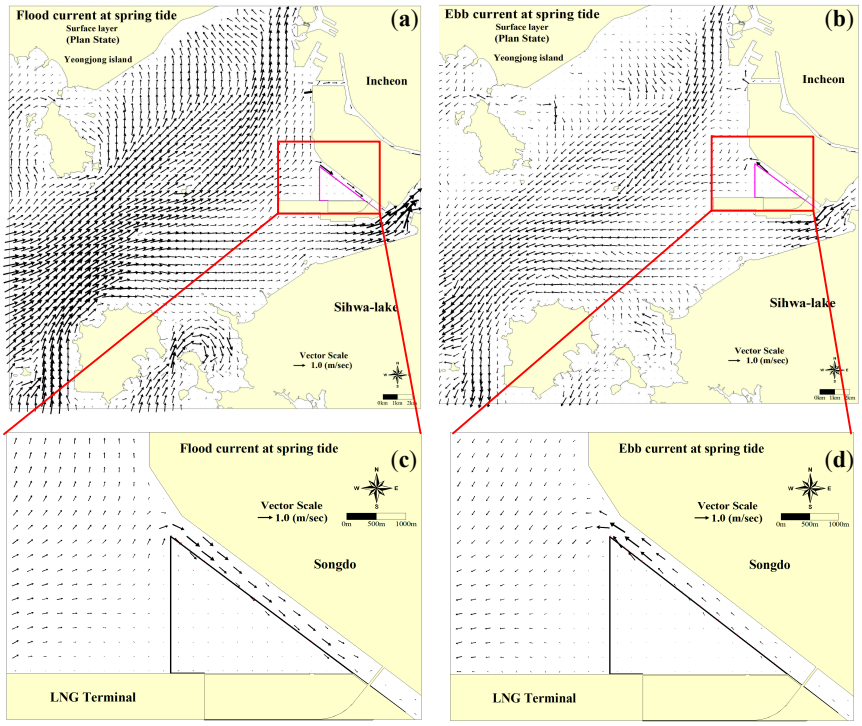

Figure 12. Current velocity fields in case 2 with only revetments were constructed without the seawater passages installed. Current fields are shown in the enlarged views during (**a**) flood and (**b**) ebb and in the detailed domain near the LNG terminal construction site during (**c**) flood and (**d**) ebb.

In Figure 13, the current fields in case 3, additionally considering the effects of the three passages for seawater exchange on case 2, again shows that the resultant impact to the dominant current direction is minimal (Figure 13a,b). For the current velocity fields, the maximum velocities on the surface were slightly increased to 0.05–0.28 m/s compared with those in case 2. These calculated current fields considering seawater exchange via permeable revetments are directly used as inputs in predicting the oil spill based on MEDSLIK-II.

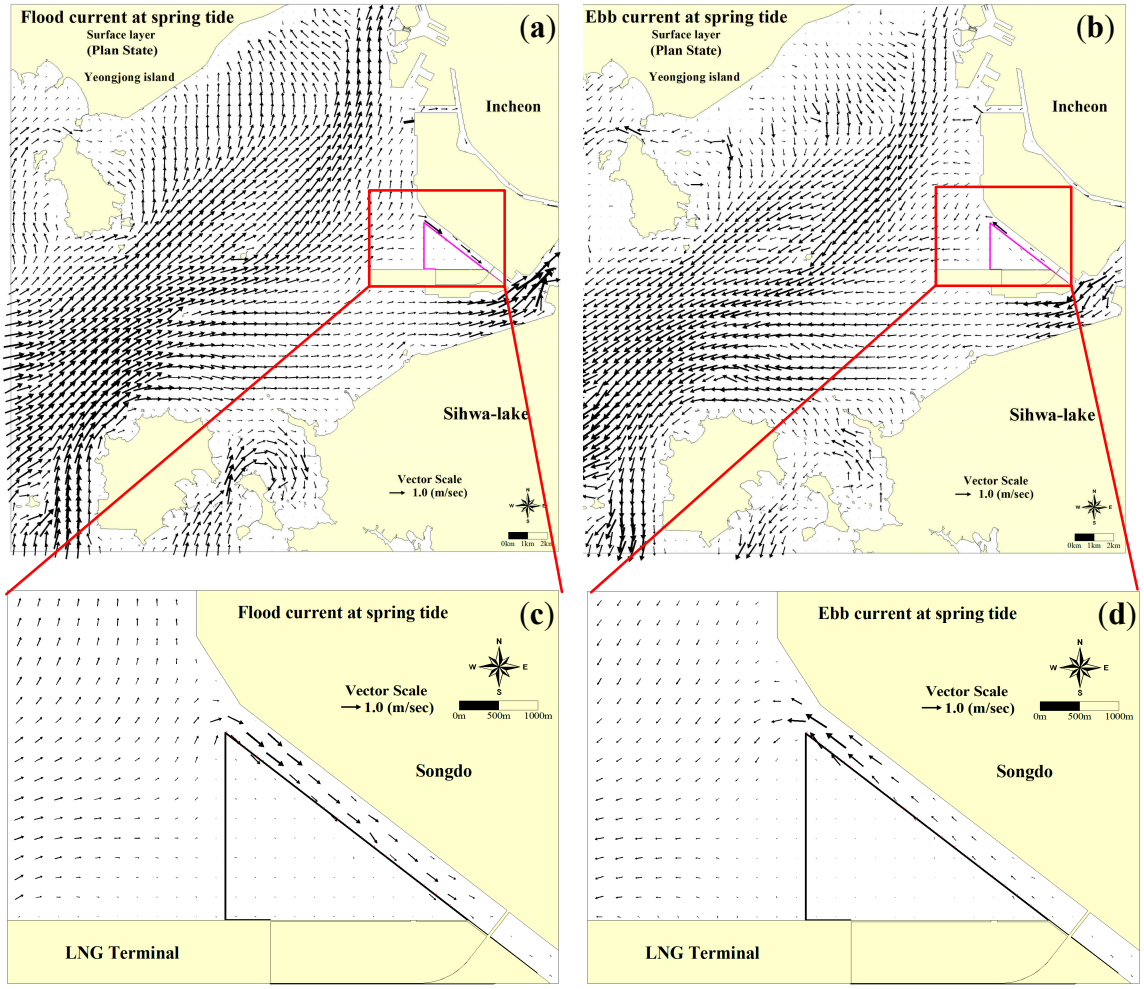

Figure 13. Current velocity fields in case 3, with both revetments and passages constructed. Current fields are shown in the enlarged views during (**a**) flood and (**b**) ebb and in the detailed domain near the LNG terminal construction site during (**c**) flood and (**d**) ebb.

3.3. Oil Spill Dispersion

3.3.1. Scenario 1

Figure 14 shows the spatiotemporal variation of the current velocity fields in Scenario 1, where the total volume of the spilled oil was the largest among the three prescribed scenarios. Scenario 1 features an initial stage of revetment construction, with only limited parts of the revetments installed. Four hours after the oil spill incident was occurred, the oil slick had stretched and advected further offshore to the west away from the Western revetment (Figure 14b). This is expected from the dominant current direction in the west near the construction site, as previously shown in Figure 11d. The oil slick reached the farthest location to the west after 6 h, at the end of the semidiurnal tidal cycle, and subsequently the advection direction is reversed toward the east (Figure 14c,d). Note that oil thickness can be directly estimated from the oil concentration fields, based on a simple

conversion. Assuming a homogeneous thickness over the spilled area, the oil thickness can be calculated by dividing oil concentration by oil density. For example, with this conversion relationship, the oil thickness in the spilled area of Figure 15c, where concentration is about 500 tonne/km^2 and LSFO density is 910 kg/m^3, may be estimated as 0.55 mm, largely comparable to typical values of oil slick thickness. Approximately 10 h after the initiation of the spill, the oil slick entered the expected reclamation area (Figure 14e). In 12 h, the oil slick is advected to the inner reclamation area and dispersed (Figure 14f). At the same time, oil slick with relatively lower oil concentration tends to be advected north following the alongshore current observed in Figure 11a. Note that the permeable revetment only allows a limited oil slick near the north edge of the western revetment (Figure 14f).

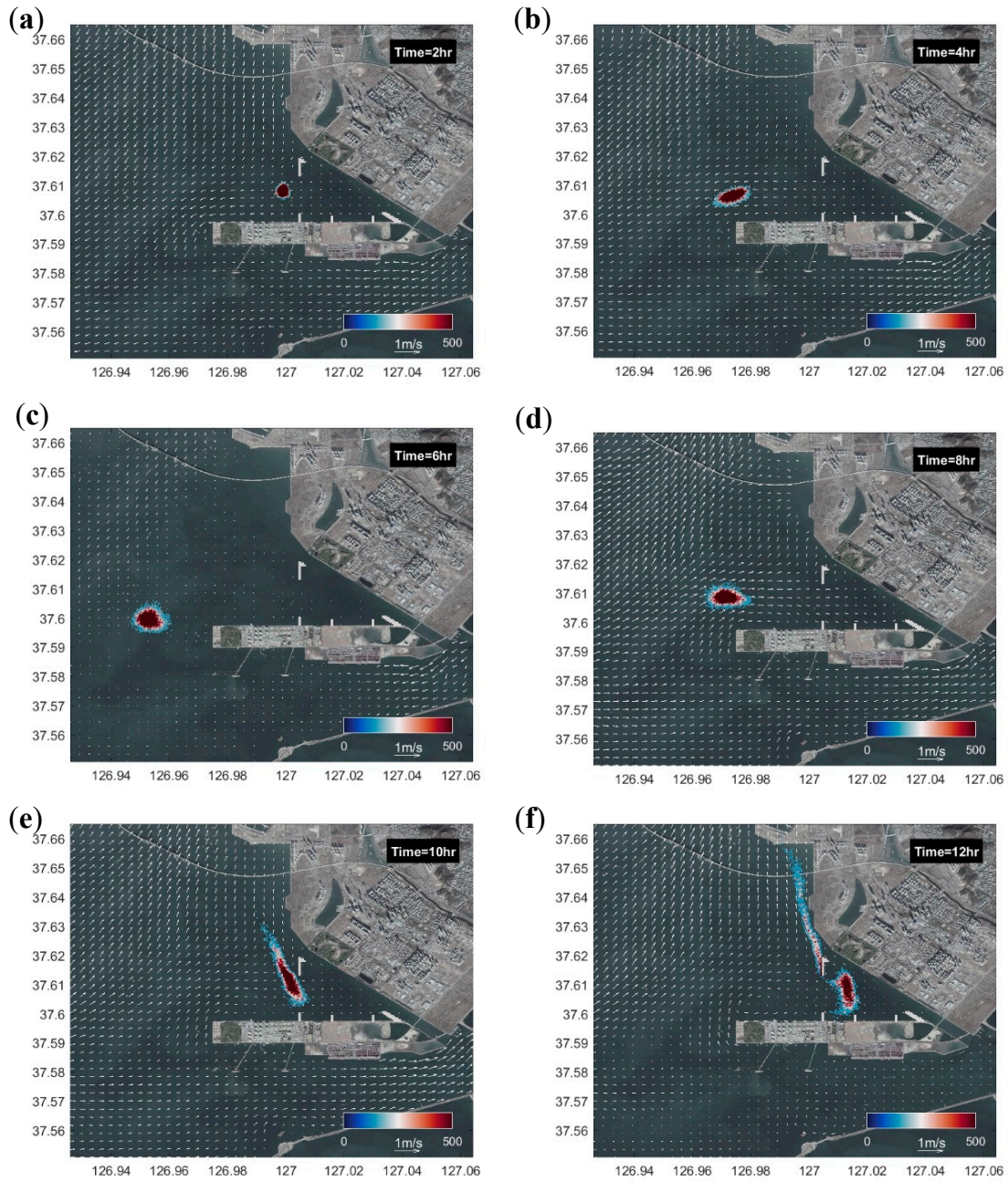

Figure 14. Temporal variation of the simulated oil concentration [tonne·km^{-2}] in (**a**) 2, (**b**) 4, (**c**) 6, (**d**) 8, (**e**) 10, and (**f**) 12 h after initiation in Scenario 1. Background vectors visualize tidal current fields.

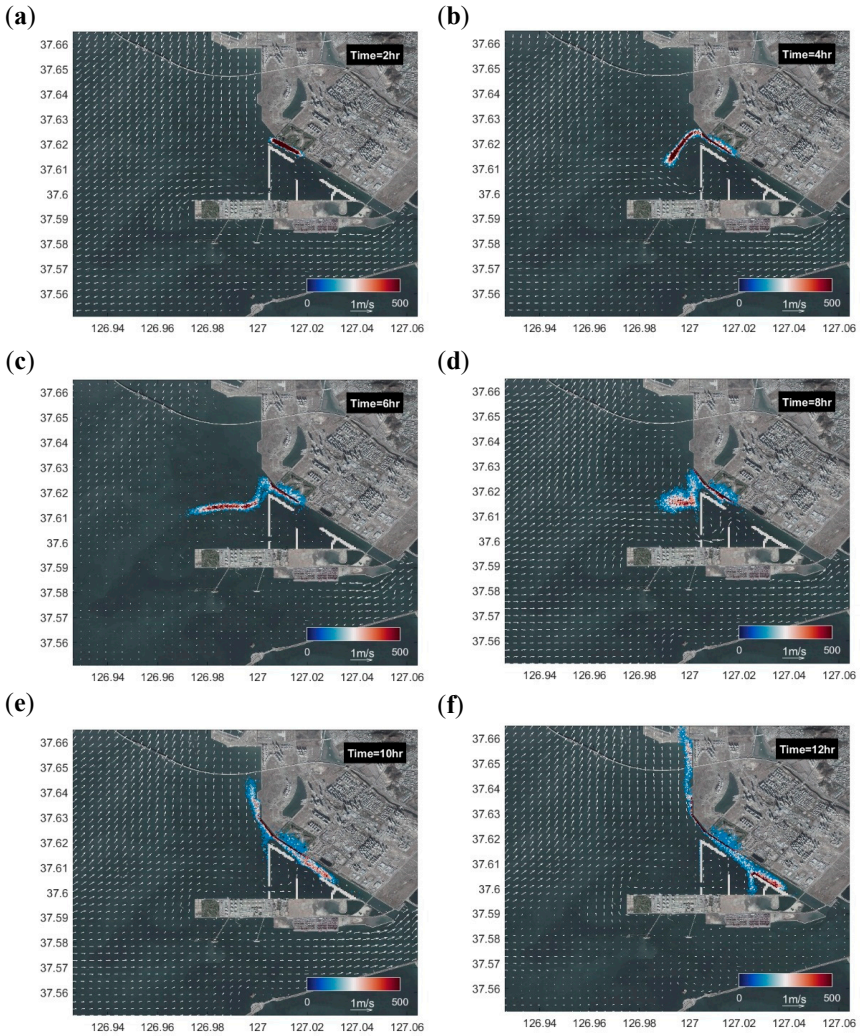

Figure 15. Temporal variation of the simulated oil concentration [tonne·km^{-2}] in (**a**) 2, (**b**) 4, (**c**) 6, (**d**) 8, (**e**) 10, and (**f**) 12 h after initiation in Scenario 2. Background vectors visualize tidal current fields.

3.3.2. Scenario 2

Unlike Scenario 1, in Scenario 2, the initiation of the oil spill occurs near the northern part of the waterway, as shown in Figure 15. In this case, the oil slick is initially attached along the coasts within the waterway (Figure 15a). As the tidal cycle approaches the maximum ebb, the oil slick is stretched off the waterway to the north and further advected to the southwest (Figure 15c) following the dominant tidal currents, as depicted in Figures 11b and 12b. The oil slick is advected more to the west until the reversal in the direction of the tidal currents occurred (Figure 15c). Then, due to the relatively weak permeability of the revetment, the oil slick is concentrated to form a more circular shape (Figure 15d). Moreover, the oil slick is not advected inside the reclamation area until 12 h after the oil spill initiation. After 8 and 12 h, the oil slick is stretched and attached along the coasts to cover approximately 5.2 and 9.8 km in length, respectively.

Samaras et al. [30] modified the MEDSLIK-II to better reflect the local coast type and beach properties, which is one of the most important many interrelated environmental drivers in predicting the oil behavior at the shoreline [31]. Specifically, Samaras et al. [30] revised the release criteria for beached particles, proposed a more detailed shoreline discretization, and adopted the Oil Holding approach to improve the prediction of C_C (Equation (9)) in MEDSLIK-II. Samaras et al. [30] explicitly showed that the oiled shoreline modeled with the modified version better matched satellite observation. With these modifications applied, the current model has the potential to enhance the predictability of

oil behavior near the coastline in the future works. The accurate prediction of the expected length of the oiled shoreline is important to evaluate the clean-up costs correctly. For example, Etkin [32] reported that about 6000 USD/tonne are needed to clean-up an oiled shoreline of 2–5 km, while about 11,000 USD/tonne are needed for the recovery of an oiled shoreline of 8–15 km.

3.3.3. Scenario 3

In Scenario 3, the oil spill originated at a location close to that in Scenario 2, near the northern part of the waterway. In 4 h, the oil slick is advected to the southwest with a sharp turnover immediately off the waterway, mainly due to the maximum ebb current (Figure 16b). Here, the shape of the oil slick is similar to that in Scenario 2, except for the oil concentration. The oil concentration during the maximum ebb in Scenario 3 is generally lower because the total leakage volume is less than half of that in Scenario 2. Moreover, comparison of Figures 15f and 16f showed that the oil slick only entered inside the expected reclamation area in scenario 2, where the revetment construction was partially completed. This suggests that an emergent oil-fence installation may be required in scenario 2 to prevent possible hazards caused by the oil penetrating during the further reclamation process. Nevertheless, the overall tendency of advection, diffusion, and transformation of the surface oil is very similar during the entire duration of 12 h (Figure 16).

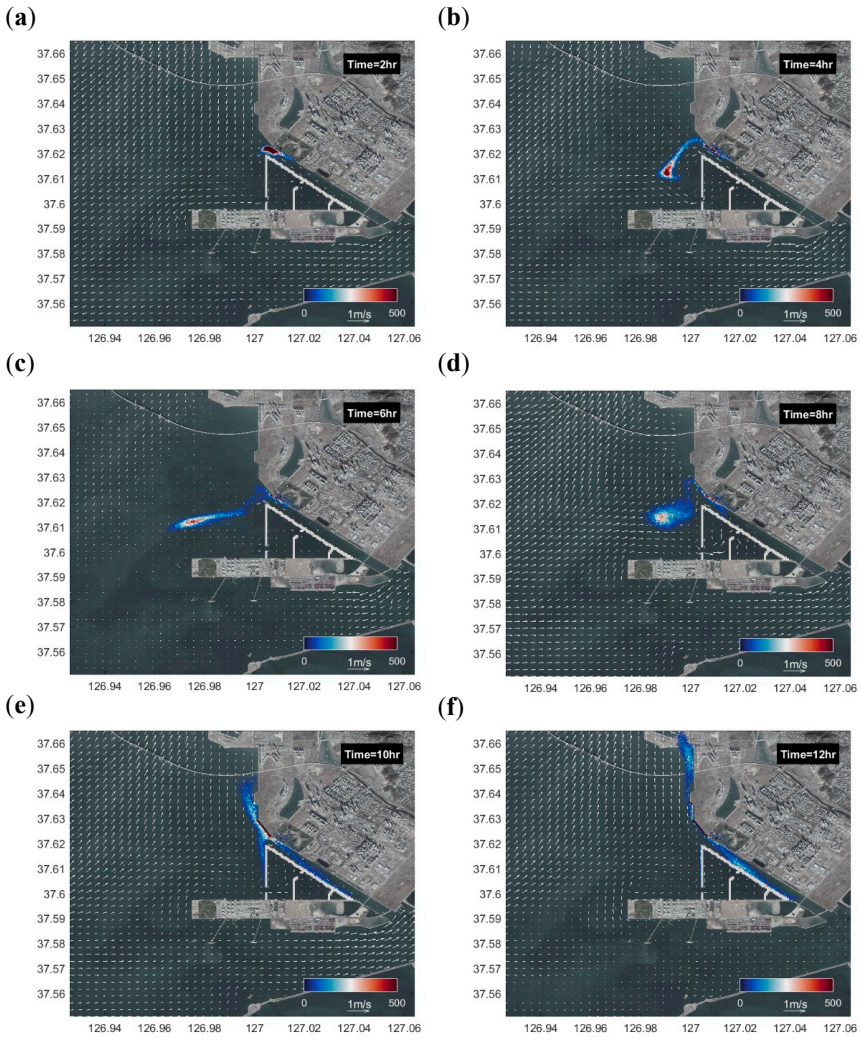

Figure 16. Temporal variation of the simulated oil concentration [tonne·km^{-2}] in (**a**) 2, (**b**) 4, (**c**) 6, (**d**) 8, (**e**) 10, and (**f**) 12 h after initiation in Scenario 3. Background vectors visualize tidal current fields.

4. Conclusions

In the current study, an oil spill modeling system was proposed by coupling the EFDC for computing tidal elevation and current fields, which were inputted to MEDSLIK-II [17] to predict oil slick advection-diffusion and transformation processes. Wind velocity fields, computed based on extreme value analysis utilizing the probability density function of a 5-year easterly wind, were also fed into MEDSLIK-II, accounting for the atmospheric condition. The current oil spill modeling system was applied to the three ship collision scenarios generated based on the proposed construction plan of the Songdo LNG terminal on reclaimed land in South Korea. The numbers, locations, types, and the sizes of the construction vessels in the three scenarios were varied to closely reflect the three distinguished construction phases (phase 1, 2, and 3) depending on the progressive time frames of construction. Prior to the MEDSLIK-II simulation, the current fields and the residual current (i.e., current field averaged over a tidal cycle) were successfully verified based on the observation data. The effects of permeable revetments, required for reclamation, on the currents were also investigated. For each scenario, the simulated results showed distinct patterns in the advection, dispersion, and transformation of the oil slick. It can be deduced from the simulated results that the oil absorption into the coast, which causes immense damage to coastal communities, is highly dependent on the tidal currents, volume of oil spilled, and nearby construction activities.

The current modeling results have a potential to be further refined to better reflect the local beach properties by revising the release criteria for beached particles and by discretizing shorelines in more detail based on the categorized coast types. An indoor laboratory experiment is also required to precisely identify the weathering process of spilled oil and thereby determine the parameters involved in the modelling procedure. In this regard, a depth-varying oceanographic flow condition can be practically reproduced by adopting the state-of-art wavemaker theory and bottom treatment [33,34]. Through accurate prediction of the oiled shoreline, a hazard mitigation plan, such as an emergent oil-fence installation, can be effectively incorporated into the modeling results to minimize the environmental impact of oil spill accidents. Consequently, the proposed modeling system turns out to successfully provide an operational tool for simulating likely schemes of oil spill accidents within the construction time frame.

Author Contributions: Conceptualization, S.S. and J.-C.C.; methodology, B.N. and S.S.; validation, B.N. and S.S.; formal analysis, B.N. and S.S.; investigation, B.N. and S.S.; writing—original draft preparation, B.N.; writing—review and editing, B.N. and S.S.; visualization, B.N. and S.S.; supervision, S.S.; funding acquisition, S.S. and J.-C.C. All authors have read and agreed to the published version of the manuscript.

Funding: This work was supported by the research project (2019R1A2C1089109, 2019H1D3A1A0107072213, & 2020R1C1C100513311) through the National Research Foundation of Korea (NRF) funded by the Ministry of Education, and by the design project funded by Daewoo E&C.

Institutional Review Board Statement: Not applicable.

Informed Consent Statement: Not applicable.

Data Availability Statement: The data presented in this study are available on request from the corresponding author.

Acknowledgments: The authors are grateful to Mirae Ocean Corporation for providing simulated and analyzed EFDC data with processed figures that had been a part of design project under the contract with Daewoo E&C.

Conflicts of Interest: The authors declare no conflict of interest.

References

1. Xie, C.; Deng, J.; Zhuang, Y.; Sun, H. Estimating oil pollution risk in environmentally sensitive areas of petrochemical terminals based on a stochastic numerical simulation. *Mar. Pollut. Bull.* **2017**, *123*, 241–252. [CrossRef]
2. Ribotti, A.; Antognarelli, F.; Cucco, A.; Falcieri, M.F.; Fazioli, L.; Ferrarin, C.; Olita, A.; Oliva, G.; Pes, A.; Quattrocchi, G. An Operational Marine Oil Spill Forecasting Tool for the Management of Emergencies in the Italian Seas. *J. Mar. Sci. Eng.* **2019**, *7*, 1. [CrossRef]
3. Lee, K.-H.; Kim, T.-G.; Cho, Y.-H. Influence of Tidal Current, Wind and Wave in Hebei Spirit Oil Spill Modeling. *J. Mar. Sci. Eng.* **2020**, *8*, 69. [CrossRef]
4. Beegle-Krause, C.J. GNOME:NOAA's next-generation spill trajectory model. In Proceedings of the OCEANS'99 MTS/IEEE, Riding the Crest into the 21st Century, Seattle, WA, USA, 13–16 September 1999; pp. 1262–1266.
5. Duran, R.; Romeo, L.; Whiting, J.; Vielma, J.; Rose, K.; Bunn, A.; Bauer, J. Simulation of the 2003 Foss Barge-Point Wells Oil Spill: A Comparison between BLOSOM and GNOME Oil Spill Models. *J. Mar. Sci. Eng.* **2018**, *6*, 104. [CrossRef]
6. Castanedo, S.; Medina, R.; Losada, I.J.; Vidal, C.; Mendez, F.J.; Osorio, A.; Juanes, J.A.; Puente, A. The Prestige oil spillin Cantabria Bay of Biscay. Part I: Operational forecasting systemfor quick response, risk assessment, and protection of natural resources. *J. Coast. Res.* **2006**, *22*, 1474–1489. [CrossRef]
7. Reed, M.; Gundlach, E.; Kana, T. A coastal zone oil spill model: Development and sensitivity studies. *Oil Chem. Pollut.* **1989**, *5*, 411–449. [CrossRef]
8. Reed, M.; Aamo, O.M.; Daling, P.S. Quantitative analysis of alternate oil spill response strategies using OSCAR. *Spill Sci. Technol. Bull.* **1995**, *2*, 67–74. [CrossRef]
9. Spaulding, M.; Kolluru, V.; Anderson, E.; Howlett, E. Application of three-dimensional oil spill model (WOSM/OILMAP) to hindcast the Braer spill. *Spill Sci. Technol. Bull.* **1994**, *1*, 23–35. [CrossRef]
10. Al-Rabeh, A.H.; Lardner, R.W.; Gunay, N. Gulfspill Version 2.0: A software package for oil spills in the Arabian Gulf. *Environ. Modell. Softw.* **2000**, *15*, 425–442. [CrossRef]
11. Lehr, W.; Jones, R.; Evans, M.; Simecek-Beatty, D.; Overstreet, R. Revisions of the ADIOS oil spill model. *Environ. Model. Softw.* **2022**, *17*, 189–197. [CrossRef]
12. Daniel, P.; Marty, F.; Josse, P.; Skandrani, C.; Benshila, R. Improvement of Drift Calculation in Mothy Operational Oil Spill Prediction System. *Int. Oil Spill Conf. Proc.* **2003**, *1*, 1067–1072. [CrossRef]
13. Carracedo, P.; Torres-López, S.; Barreiro, M.; Montero, P.; Balseiro, C.; Penabad, E.; Leitao, P.; Pérez-Muñuzuri, V. Improvement of pollutant drift forecast system applied to the Prestige oil spills in Galicia Coast (NW of Spain): Development of an operational system. *Mar. Pollut. Bull.* **2006**, *53*, 350–360. [CrossRef] [PubMed]
14. Pollani, A.; Triantafyllou, G.; Petihakis, G.; Nittis, K.; Dounas, C.; Christoforos, K. The Poseidon operational tool for the prediction of floating pollutant transport. *Mar. Pollut. Bull.* **2001**, *43*, 270–278.
15. Hackett, B.; Breivik, Ø.; Wettre, C. Forecasting the Drift of Objects and Substances in the Ocean. In *Ocean Weather Forecasting*; Springer: Dordrecht, The Netherlands, 2006; pp. 507–523. [CrossRef]
16. Socolofsky, S.A.; Adams, E.E.; Boufadel, M.C.; Aman, Z.M.; Johansen, Ø.; Konkel, W.J.; Lindo, D.; Madsen, M.N.; North, E.W.; Paris, C.B. Intercomparison of Oil Spill Prediction Models for Accidental Blowout Scenarios with and without Subsea Chemical Dispersant Injection. *Mar. Pollut. Bull.* **2015**, *96*, 110–126. [CrossRef] [PubMed]
17. De Dominicis, M.; Pinardi, N.; Zodiatis, G.; Lardner, R. MEDSLIK-II, a Lagrangian marine surface oil spill model for short-term forecasting—Part 1: Theory. *Geosci. Model. Dev.* **2013**, *6*, 1851–1869. [CrossRef]
18. De Dominicis, M.; Pinardi, N.; Zodiatis, G.; Archetti, R. MEDSLIK-II, a Lagrangian marine surface oil spill model for short-term forecasting—Part 2: Numerical simulations and validations. *Geosci. Model. Dev.* **2013**, *6*, 1871–1888. [CrossRef]
19. Coppini, G.; De Dominicis, M.; Zodiatis, G.; Lardner, R.; Pinardi, N.; Santoleri, R.; Colella, S.; Bignami, F.; Hayes, D.R.; Soloviev, D. Hindcast of oil-spill pollution during the Lebanon crisis in the Eastern Mediterranean, July–August 2006. *Mar. Pollut. Bullet.* **2011**, *62*, 140–153. [CrossRef]
20. Neves, A.; Pinardi, N.; Martins, F.; Janeiro, J.; Samaras, A.; Zodiatis, G.; De Dominicis, M. Towards a common oil spill risk assessment framework adapting ISO 31000 and addressing uncertainties. *J. Env. Manag.* **2015**, *159*, 158–168. [CrossRef]
21. Daewoo E&C. *Design Report on the LNG Terminal Construction of the Incheon New Port*; 2019; Unpublished Internal Report in Korean.
22. Hamrick, J.M. A Three-Dimensional Environmental Fluid Dynamics Computer Code: Theoretical and computational aspects. In *Special Report in Applied Marine Science and Ocean Engineering*; Virginia Institute of Marine Science; College of William & Mary: Williamsburg, VA, USA, 1992; No. 317.
23. Yang, Z.; Hamrick, J.M. Variational inverse parameter estimation in a cohesive sediment transport model: An adjoint approach. *J. Geophys. Res.* **2003**, *108*, 3055. [CrossRef]
24. Mellor, G.L.; Yamada, T. Development of a turbulence closure model for geophysical fluid problems. *Rev. Geophys.* **1982**, *20*, 851–875. [CrossRef]
25. Galperin, B.; Kantha, L.H.; Hassid, S.; Rosati, A. A Quasi-equilibrium Turbulent Energy Model for Geophysical Flows. *J. Atmos. Sci.* **1988**, *45*, 55–62. [CrossRef]

26. Mackay, D.; Paterson, S.; Trudel, B. *A mathematical model of oil spill behavior. Report to Research and Development Division, Environment Emergency Branch, Environmental Impact Control Directorate, Environmental Protection Service*; Environment Canada: Ottawa, ON, Canada, 1980.
27. Shaw, W.J.; Trowbridge, J.H. The Direct Estimation of Near-Bottom Turbulent Fluxes in the Presence of Energetic Wave Motions. *J. Atmos. Oceanic Technol.* **2001**, *18*, 1540–1557. [CrossRef]
28. Imasato, N. What is Tide-Induced Residual Current? *J. Phys. Oceanogr.* **1983**, *13*, 1307–1317. [CrossRef]
29. Wang, H.F.; Anderson, M.P. Introduction to Groundwater Modeling. In *W.H. Freeman and Company*; Academic Press: Cambridge, MA, USA, 1982.
30. Samaras, A.G.; De Dominicis, M.; Archetti, R.; Lamberti, A.; Pinardi, N. Towards improving the representation of beaching in oil spill models: A case study. *Mar. Pollut. Bull.* **2014**, *88*, 91–101. [CrossRef] [PubMed]
31. Etkin, D.S.; French-McCay, D.; Michel, J. *Review of the State-of-the-Art on Modelling Interactions between Spilled Oil and Shorelines for the Development of Algorithms for Oil Spill Risk Analysis Modelling*; Cortlandt Manor: NewYork, NY, USA, 2007; p. 157.
32. Etkin, D. Worldwide Analysis of Marine oil Spill Cleanup Cost Factors (online). 2000. Available online: http://citeseerx.ist.psu.edu/viewdoc/download?doi=10.1.1.579.903&rep=rep1&type=pdf (accessed on 30 March 2021).
33. Kim, Y.; Son, S.; Jung, T.; Gallien, T. An analytical and numerical study of a vertically discretized multi-paddle wavemaker for generating free surface and internal waves. *Coast. Eng.* **2021**, *165*, 103840. [CrossRef]
34. Jung, T.; Son, S. Active tsunami generation by tectonic seafloor deformations of arbitrary geometry considering rupture kinematics. *Wave Motion* **2021**, *100*, 102683. [CrossRef]